Precision Engineering 53 (2018) 236–247

Contents lists available at ScienceDirect

Precision Engineering

journal homepage: www.elsevier.com/locate/precision

Design and characterization of a two-axis, flexure-based nanopositioning stage with 50 mm travel and reduced higher order modes☆

Nilabh K. Roy, Michael A. Cullinan*

Department of Mechanical Engineering, The University of Texas at Austin, Austin, 78712, USA

ARTICLE INFO

Keywords:
Nanopositioning
Double parallelogram
Flexure stage
Underconstraint eliminator
50 mm travel

ABSTRACT

Long range, high precision, XY stages have a multitude of applications in scanning probe microscopy, lithography, micro-AM, wafer inspection and other fields. However, finding cost effective precision motion stages with a range of more than 12 mm with a precision better than one micron is a challenge. This study presents parametric design of the two XY flexure-based stages with a travel ranges of up to 50 mm and sub-micron resolution. First, the fabrication and testing of a two-axis double parallelogram flexure stage is presented and the results obtained from FEA and experimental measurements are shown to be in good agreement with the analytical predictions for this stage. A modified stage design with reduced higher order modes and same range, is also presented. This modified design is shown to be capable of achieving an open loop resolution of 100 nm with a travel range of greater than 50 mm. Higher order modes of the modified stage have been shown to be shifted from 25 Hz in the double parallelogram flexure (DPF) stage to over 86 Hz in the modified DPF stage making it much simpler to design a high speed (> 10 Hz) controller for the modified stage.

1. Introduction

Long range XY stages with high precision have a number of applications in fields such as lithography [1,2], scanning probe microscopy [3], atomic force microscopy [4] to molecular spectroscopy [5], nanometrology [6], biological cell manipulation [7], micro additive manufacturing processes [8], wafer inspection, chip packaging [9], optics [10], and micro-machining. There have been a number of studies pertaining to the design of precision motion stages with range of a few mm [11–13]. However, achieving motion range higher than 10 mm with sub-micron resolution has been a challenge in designing of nanopositioning stages. Mounting a fine flexure based mechanism on top of a coarse positioning system is one of the common methods to overcome this difficulty. However, this approach makes the system complex, bulky, expensive and more challenging to control as there are more variables to control simultaneously in the system. This study is focused towards the design and development of an XY precision stage with a range of 50 mm along each axis which pushes the higher order resonance modes of the stage out to more than one order-of-magnitude greater than the fundamental mode of this stage. This result is achieved by eliminating the underconstraint in traditional double parallelogram flexure based stages for the stage presented in this paper. By pushing the higher order, uncontrolled resonance modes out in this new stage design it is possible to design a controller for the new stage that allows the new stage design to operate well beyond its fundamental frequency thus significantly improving the speed and dynamic performance of these types of stages.

To achieve a long motion range with sub-micron step resolution and high accuracy, flexure bearings have been the favored alternative over contact based linear bearings such as ball screw and lead screw based stages employing ball bearings or roller bearings due to the zero friction, zero backlash, and minimal hysteresis of flexure bearings [14,15]. Although magnetic bearings and air bearings can achieve long motion range with resolutions less than 10 nm [16], their high costs make them infeasible for research labs. In addition to being cost effective, flexure bearings also provide design simplicity and freedom to optimize the design to one's requirements. Flexure bearing designs for scanning in two directions can be divided into two broad categories: (1) Serial kinematic designs and (2) Parallel kinematic designs (see Fig. 1). Both these designs have their advantages and disadvantages. A serial kinematic design is obtained either by stacking one bearing in series with the other bearing or by nesting one of them inside the other [17]. Although this design makes the structure compact, it adds inertia to the base bearing. Thus, the base bearing has a lower resonance frequency and consequently, a smaller bandwidth along the base bearing primary motion axis. Secondly, it is difficult to measure and calibrate the

☆ This paper was recommended by Associate Editor Dannis Brouwer.

* Corresponding author at: University of Texas at Austin, Department of Mechanical Engineering, 204 E. Dean Keeton Street, Stop C2200, ETC 4.154, Austin, TX, 78712-1591, USA.
E-mail address: Michael.Cullinan@austin.utexas.edu (M.A. Cullinan).

https://doi.org/10.1016/j.precisioneng.2018.04.007
Received 8 September 2017; Received in revised form 10 April 2018; Accepted 11 April 2018
Available online 17 April 2018

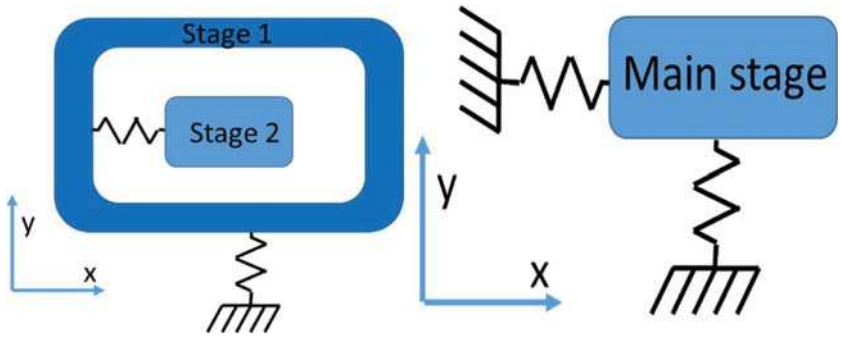

Fig. 1. a) Serial Kinematic design with one stage nested inside the second stage b) Parallel kinematic design.

parasitic motion in serial stages [18]. And lastly, serial designs often have internal degrees of freedom leading to unwanted parasitic eigenmodes. A parallel kinematic design has the bearings attached to the main stage in parallel, i.e., the bearing along each axis is mounted to the ground, thus reducing the inertia of the moving stage. This leads to high resonant frequencies and identical dynamics along both axes. Parallel kinematic designs also have high mechanical stiffness along actuation direction leading to a higher motion accuracy [19]. A parallel kinematic structure thus provides a better alternative in achieving high speed long range motion along both axes with good accuracy.

A number of two-dimensional flexure-based parallel-kinematic positioning stages have been proposed by researchers. In previous work, double parallelogram flexure (DPF) designs have been employed to achieve centimeter range motions [11,12]. In general, a DPF stages lead to an increased range and reduced parasitic errors compared to a single parallelogram flexure stage [20]. However, DPF suffers from a drawback which is that it enables both the intermediate stages and final stages to have same degrees of freedom (DOF). This leads to unwanted degrees of freedom on the intermediate stages which may interfere with the controller performance if the corresponding modes (associated with resonances of intermediate stages) fall within the operating frequency range [21]. Many studies have proposed solutions to this problem including double tilted beam flexure bearing [22] and external linkage designs [23]. However, both these solutions suffered from drawbacks; double tilted beam flexure bearing design suffered from altered DOF and high non-diagonal coupling between design parameters and functional requirements while the external linkage design led to an increase in footprint and altered the dynamics of the stage. More recently, a nested linkage design based upon the external linkage design for eliminating the underconstraint has been presented in [24]. This design has been shown to work effectively in eliminating the underconstraint for a single unit (Fig. 1).

In addition to the flexures being able to achieve the desired range, it is required to use actuators that meet the design criteria of range and precision. Electromagnetic actuators or voice coil actuators (VCAs) are widely used in long-travel, flexure-based parallel XY stages since VCAs are capable of delivering a frictionless 50 mm stroke along with a fine resolution [25]. The resolution is dictated either by the resolution of the input power supply or by the noise of the power supply depending upon which one is larger.

A DPF bearing design for the XY stage was presented in [25] to achieve a 50 mm desired motion range along each axis. The stage design is a two-level design and modular in nature, thus reducing any coupling $^{\text{between}}$ the two motion axes and making the controller design easier as the control for each axis can be developed as a single input single output (SISO) system instead of developing a multi input multi output (MIMO) control system. This design, however, has additional degrees of freedom of the intermediate stage which can interfere with the design and operation of a controller. Thus, we also present a modified design of the stage to move out the expected uncontrolled resonances of the intermediate stage beyond the operating range. These two designs are discussed in detail in the following sections and they are compared on the basis of FEA results. Afterwards, prototypes for both stages are developed and their static and dynamic performances are compared with each other and with the FEA predictions.

2. Design and analysis

2.1. DPF design of XY stage

The XY precision stage design is based on double parallelogram flexures due to their large elastic deformations contributing to a long motion range. Deformation of a simple double parallelogram unit is shown in Fig. 2. Applying the boundary conditions to the unit, the stiffness along tangential (along $\hat{e}_t$ as shown in Fig. 2) and axial directions (along $\hat{e}_a$) can be obtained by Eqs. (1) and (2) [20]

$$K_a \approx \frac{1}{\left(b^2 + \frac{9}{25}x_t^2\right)} \cdot \frac{12EI}{l} \tag{1}$$

$$K_t \approx \left[12 - \frac{3}{100}\left(\frac{F_a l^2}{EI}\right)^2\right] \cdot \frac{EI}{l^3} \tag{2}$$

where b, l, and E are the flexure width, beam length, and Young's modulus, respectively, I is the second moment of area of the flexure beam, F_a is the magnitude of axial force on the beam and x_t is the tangential displacement of the beam. For small tangential displacements i.e. for $x_t \ll b$, the axial stiffness estimate can be modified and is given by Eq. (3). And for tangential stiffness estimation, the applied force on the beams is purely tangential and hence, the tangential stiffness estimate can be obtained by (4)

$$K_a \approx \frac{1}{(b^2)} \cdot \frac{12EI}{l} \tag{3}$$

$$K_t \approx \frac{12EI}{l^3} \tag{4}$$

It is to be noted however that these estimates are for small displacement regime. As the tangential displacements become larger, the estimates need to be revised and can be accurately found using Eqs. (1)

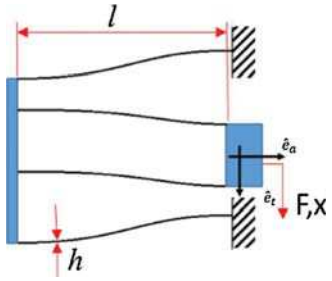

Fig. 2. Schematic of a double parallelogram flexure(DPF) mechanism.

Table 1
Structural parameters, analytical stiffness and one-directional range for XY stage- design 1.

Parameter	Value	Parameter	Value
Effective Length of beams (l)	93.6 mm	Factor of safety	2
Thickness of beams (h)	0.5 mm	x_{max} (FOS = 2)	20.5 mm
		x_{max}(FOS = 1)	41 mm
Width of beams (b)	12.7 mm	Tangential Stiffness, $K_x(=K_y)$	833 N/m

and (2). Generally, the length of the beam, l is considerably larger than the width of the beam, b making the axial stiffness, K_a significantly greater than the tangential stiffness which leads to extremely low compliance along $\hat{e_a}$ and, thus, aids in reducing parasitic motion of the stage. The maximum displacement of the flexure unit is associated with the maximum stress induced in the flexure beam. This maximum stress in a flexure beam with rectangular cross-section can be obtained using the bending stress equation, $\sigma = \frac{My}{I}$. Using a given factor of safety, the maximum displacement in one direction can be obtained by using the maximum stress developed in a beam bending

$$x_{max} = \sigma_y * \frac{l^2}{3*E*h*FOS} \tag{5}$$

where, σ_y is the yield limit of the material of the beams, E is the Young's modulus of the material, h is the thickness of the beam and FOS is the desired factor of safety for the design. From Eq. (5), displacement of the stage is directly proportional to the square of length of the beams and inversely proportional to the thickness of the beams. Thus, to achieve a long motion range, longer flexures with smaller thicknesses are preferred. However, the minimum thickness of the beam is limited by the manufacturing tolerance of the waterjet cutting tool. Generally, that leaves only the length of the beams that can be modulated to achieve the desired range for a given material of the beam.

The two level XY design of the stage is based on the designs presented in [26,27]. The corner modules on each level of the stage are grounded while one of the center modules on each level of the stage is connected to the designated VCA for respective axes. The motion of the stage along the actuation direction is guided by a) four DPF units located at the corners of the level that is being acted upon by the actuator and b) two center DPF units on the other level which is mounted orthogonally in a plane parallel to the first level's plane. Thus, a decoupled two-dimensional translation is achieved by the XY stage. Overall stiffness along each axis is calculated by estimating the stiffness of combinations of DPF units. Each axis motion is facilitated by six DPF units in parallel and, thus, stiffness along each axis is given by

$$K_{x,y} = 6*K_t = \frac{6Ebh^3}{l^3} \tag{6}$$

Modular design of the stage is cost effective both in manufacturing costs and maintenance convenience/costs. Structural dimensions of the stage including length of the beams (l), width of the beams (b) and thickness of the beams (h) have been selected (Table 1) to achieve the desired range, stiffness, and compactness. Using Al 7075 as the material for the flexures, (E = 71.7 GPa, σ_y = 503 MPa, and ρ = 2810 kg/m^3) with a factor of safety(FOS) of 2 (to account for manufacturing defects and assembly stack up error and so on), one directional range is found to be 20.5 mm providing a range of 41 mm along each axis. With an FOS of 1, this range is amplified to 82 mm which is higher than desired 50 mm travel range.

2.1.1. FEA results

For FEA simulations, the two levels of the stage are grounded through the mounting holes on each corner module of the stage level and the center-stages of both levels are held together rigidly. A unidirectional force input is fed to one of the voice coils for stress estimates along the voice coil actuation direction. Fig. 3 shows the deformation of the beams from their rest state when a force of 1 N and 22 N acts on the stage only along one direction through the VCA. The small displacement simulation (Fig. 3a) predicted a stiffness of 841 N/m. The maximum stress at 25.92 mm displacement was found to be 182.2 MPa (see Supplementary Fig. S3). Based on the stiffness obtained from FEA analysis, the maximum force rating of the actuator should be higher than the force estimated to produce the maximum displacement. Force at the displacement of 25.92 mm was found to be 22 N. Thus, a VCA with maximum force rating of 22 N or higher can be selected for the application provided it has a travel range > 50 mm. A higher force rated VCA is advisable to accommodate the variability in stiffness of the stage that may arise due to waterjet cutting and assembly stack up errors.

2.1.2. Physical model

In addition to the static simulations, a physical model of the system was constructed to help understand the dynamic behavior of the stage and estimate the resonant frequencies of the stage so that the control system can be developed accordingly keeping in mind the bandwidth of the stage. To obtain the resonant frequencies, the stage is modeled as two decoupled spring mass sub-systems along the two actuation axes. And thus, the governing equations can be written in terms of moving mass (m_x and m_y) and tangential stiffness (k_x and k_y) associated with x and y axes respectively.

$$m_x\ddot{x} + k_x x = F_x;$$
$$m_y\ddot{y} + k_y y = F_y; \tag{7}$$

In state space form; this can be represented as

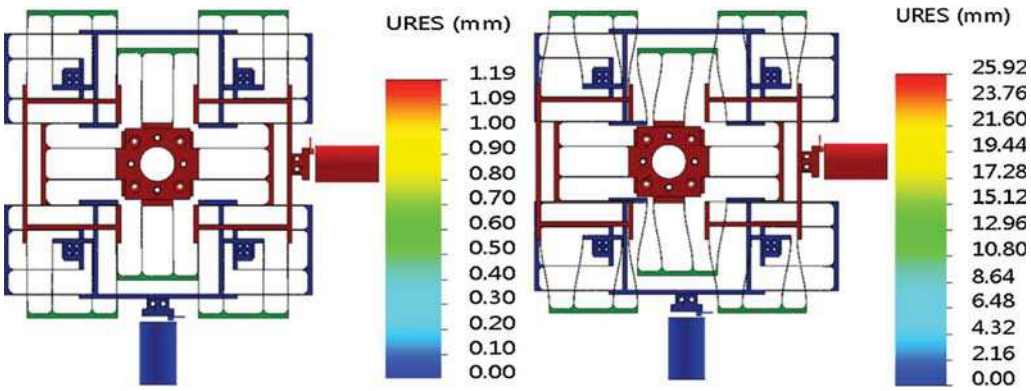

Fig. 3. Static FEA simulation of deformation induced by an input force of a) 1 N and b) 22 N.

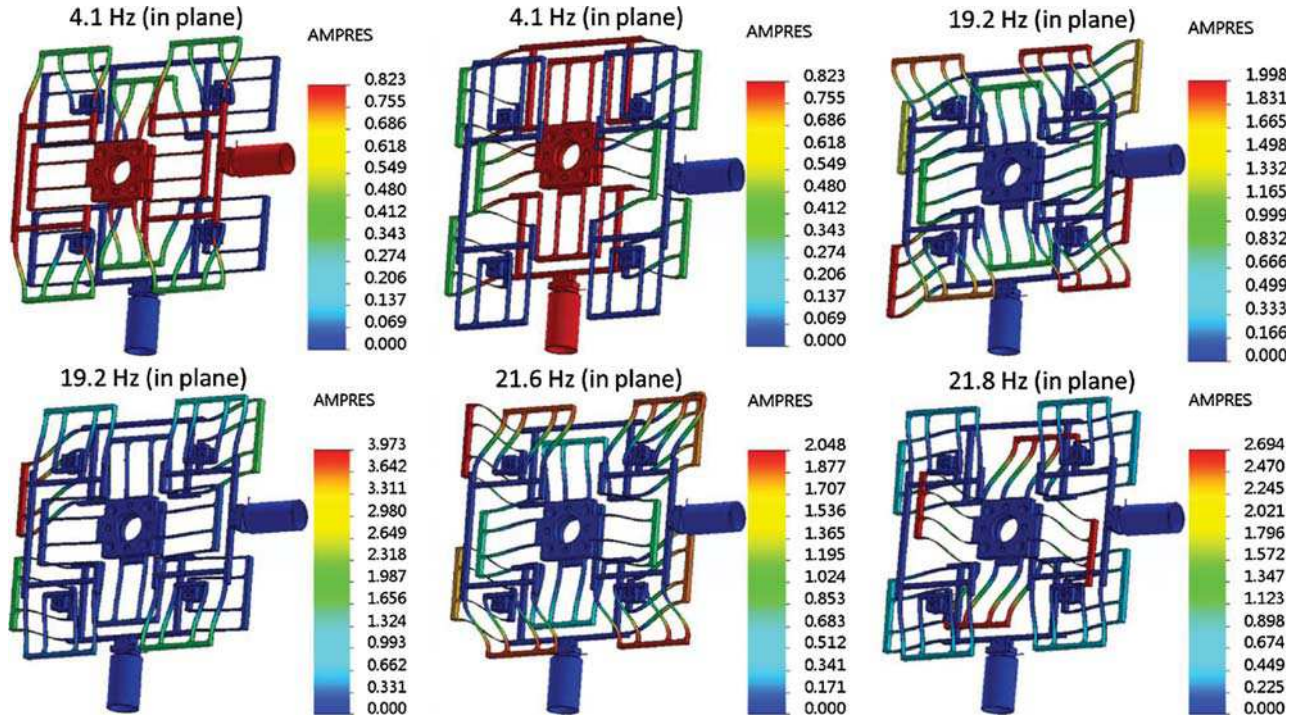

Fig. 4. First-six resonant mode shapes and resonance frequencies of the XY stage.

$$\begin{bmatrix} \dot{x} \\ \dot{v}_x \\ \dot{y} \\ \dot{v}_y \end{bmatrix} = \begin{bmatrix} 0 & 1 & 0 & 0 \\ -\frac{k_x}{m_x} & 0 & 0 & 0 \\ 0 & 0 & 0 & 1 \\ 0 & 0 & -\frac{k_y}{m_y} & 0 \end{bmatrix} \begin{bmatrix} x \\ v_x \\ y \\ v_y \end{bmatrix} + \begin{bmatrix} 0 & 0 \\ 1 & 0 \\ 0 & 0 \\ 0 & 1 \end{bmatrix} \begin{bmatrix} F_x \\ F_y \end{bmatrix} = Ax + Bu \tag{8}$$

Corresponding eigenvector-eigenvalue equation can be written as

$$[A - \lambda_i I]v_i = 0 \tag{9}$$

where, λ_i is the i_{th} eigenvalue and v_i is the corresponding eigenvector. Imaginary part of the eigenvalue relates to the natural frequency of the system and the eigenvectors are associated with the mode shapes.

$$Im(\lambda_i) = \omega_n^2$$

Here, $\lambda_{1,2} = \pm i\sqrt{\left(\frac{k_x}{m_x}\right)}$ $and \lambda_{3,4} = \pm i\sqrt{\left(\frac{k_y}{m_y}\right)}$. This being a symmetric stage with equal mass distribution along both x and y axes, $m_x = m_y and k_x = k_y$. This leads to the natural frequency being the same along both axes and is given by

$$\omega_n = \frac{1}{2\pi}\sqrt{\frac{k}{m}}\,Hz \tag{10}$$

From CAD model of the stage and actual moving mass of VCAs, moving mass along each axis is approximated to be 1.46 kg and using the analytical stiffness estimate of 833 N/m for the stage, the natural frequency of the stage is estimated to be 3.80 Hz for both axes. Fig. 4 shows the dynamic response of the stage and the first resonant frequency of the stage is obtained as 4.1 Hz. The dynamic FEA simulation does not consider the actual moving mass of the voice coils and hence, the first resonant frequency estimates are inflated compared to the analytical value. In addition to including the actual moving mass of the VCAs, states corresponding to the intermediate stages would have to be included in the model to capture the overall dynamics of the stage including resonances of intermediate stages and accurately predict the resonant frequencies of the stage. A comparison of these estimates with correction factors for stiffness and mass inclusion has been included in the Section 3.

From Fig. 4, the first-two mode shapes are contributed by the translations along the two working axes, respectively. The next four modes are the resonances of the individual DPF units. This suggests an uncontrolled DOF of the intermediate stage on the DPFs which causes the intermediate stage to be under-constrained as it is free to move even when the final stage is held fixed relative to the ground [19,26]. Although the first two modes fall within the desired bandwidth (25 Hz), the center-stage has actuators attached to it along the two axes and hence, they can be controlled using appropriate feedback control action. However, individual DPFs do not have any actuators attached to them which makes it difficult to control these modes of the DPFs. These modes can be damped passively by sandwiching a damping plate (a polymer plate with viscous fluid on either side or foam) between the two flexure planes [25]. Other passive damping techniques such as shunts [28] have been effective in damping out these uncontrollable resonances. The next significant resonance of the center-stage was observed at 117 Hz (shown in Fig. 5).

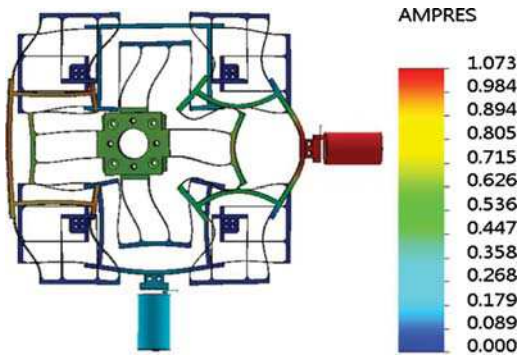

Fig. 5. Second resonance of the center-stage.

2.1.3. Experimental results

2.1.3.1. Prototype fabrication and experimental setup:. Using the results from FEA study, each flexure stage was waterjet cut out from a 12.7 mm Al 7075 plate. Al 7075 was chosen due to its high yield stress. Based on the overall dimension of the stage (443 mm × 443 mm × 31.75 mm),

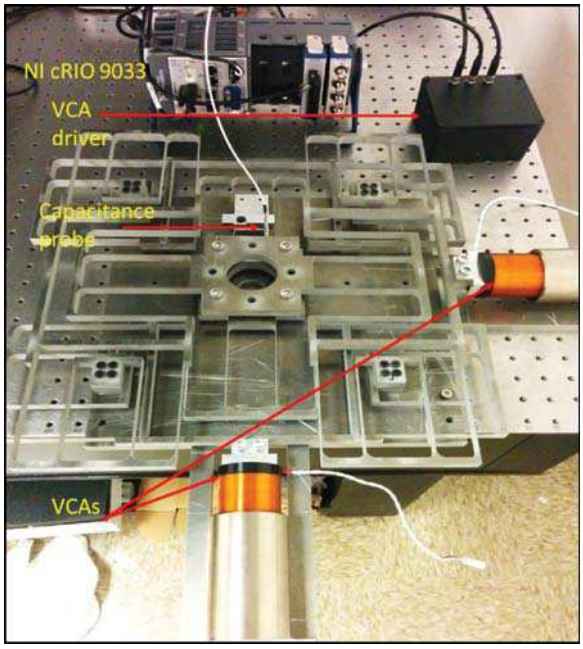

Fig. 6. Experimental setup for DPF stage design.

waterjet cutting provides a more economical alternative for cutting these flexures compared to wire EDM which has been traditionally used for cutting small flexure units. Each flexure unit is connected to a VCA with a maximum input force of 116 N and a maximum travel of 86 mm. The entire stage is mounted on a 12.7 mm plate of Al 6061 which is mounted on a vibration isolation table to remove the external noise from the stage's motion. Fig. 6 shows the assembly of the stage.

The position output for small displacements (−125 μm to 125 μm) and for dynamic characterization is measured by a capacitive sensor (model: C5-2.0, from Lion Precision) with an RMS resolution of 1 nm at 1 kHz within the measurement range of 250 μm [29]. Sensor is mounted collinearly with the working axes of the stage, respectively. For large displacements and parasitic displacement measurements, an interferometer (model: FPS3010, from Attocube Systems AG) with a resolution of 1 pm, a repeatability of 2 nm over a 10 mm travel and a working range of 2 m is used (please see Supplementary Fig. S7). For actuation and sensor measurement, a National Instruments (NI) cRIO-9033 real-time controller equipped with NI-9263 analog output module and NI-9239 analog input module, is employed to produce excitation signals and acquire sensor readings, respectively. LabVIEW VIs have been developed for data collection, actuation and to implement a real-time control for the positioning system.

2.1.3.2. Stiffness measurement:. For small displacement stiffness measurement, steps of 0.001 V are applied every two seconds to the stage and the displacement of center-stage is measured using the capacitive sensor. Analog output module, NI 9263 is a 16-bit module with output voltage range of −10 V to 10 V resulting in an output voltage resolution of 0.0003 V. To ensure that the steps are discernible from one another, an input step size of 0.001 V was selected. The small displacement stiffness of the stage can be calculated from the slope of the displacement of the stage vs input voltage graph (see zoomed in graph in Fig. 7).

The force constant (K_f) of the VCA is 14.6 N/A and the amplifier's gain(K_a) is 1.00 ± 0.14 A/V. So, the stiffness of the stage can be obtained by

$$K_{measured} = K_f * \frac{K_a}{Slope(=7701.3)*10^{-6}} \tag{11}$$

This gives a measured stiffness value of 1896 ± 265 N/m which is more than two times the stiffness value predicted by FEA. A possible cause of this could be manufacturing error due to waterjet cutting of flexures. This difference could be explained by the change in thickness of the beams from top to bottom fabricated using waterjet cutting. Flexure beams did not have the expected rectangular cross section. Instead, the cross section resembled more like a trapezoid changing the inertia of the beam and thus the stiffness estimate needs to be corrected accordingly. For a trapezoidal cross section (see Fig. 8), inertia, I_{yc} is given by

$$I_{yc} = b*(p+q)*\frac{p^2+q^2}{48} \tag{12}$$

And thus, a more accurate formula for stiffness is given by

$$K_{x,y} = 6*K_t = \frac{6*E*b*(p+q)*(p^2+q^2)}{4l_{eff}^3} \tag{13}$$

The top and bottom thicknesses of the flexure beams were found to be 0.56 ± 0.10 mm and 0.73 ± 0.08 mm respectively. The thicknesses are represented as mean ± standard deviation and were obtained using a set of 40 measurements for each thickness estimate. Using (13), the stiffness was estimated to be 1854 ± 536 N/m (using

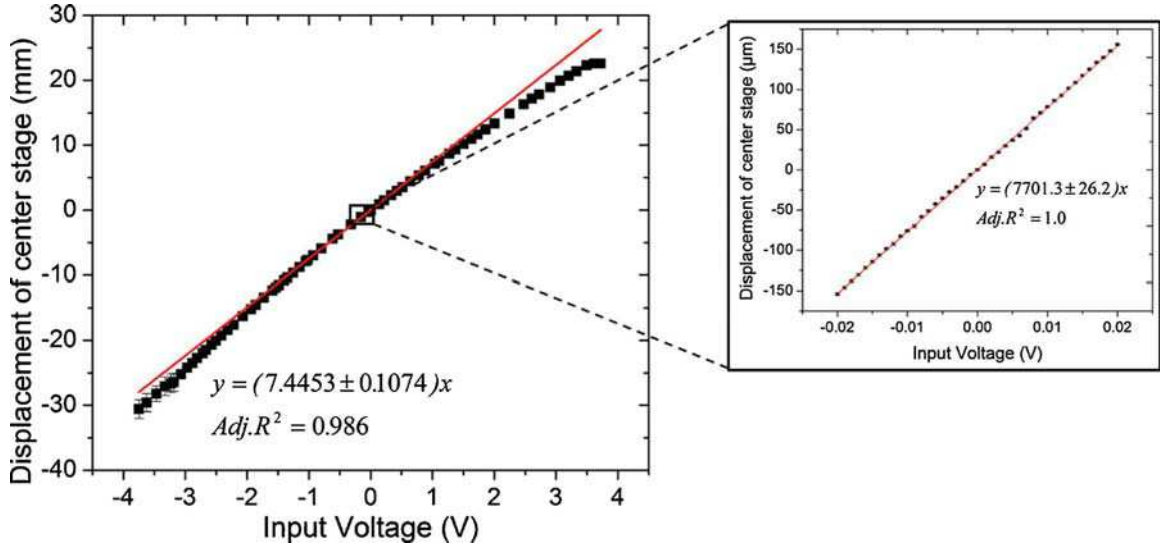

Fig. 7. Output displacement of the stage vs Input voltage.

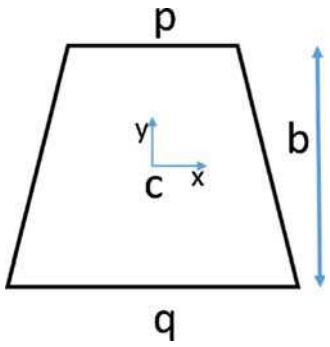

Fig. 8. A trapezoidal cross section.

original FEA estimate) which is close to the measured stiffness of the stage. A correction factor can be defined as the ratio of inertias of the trapezoidal cross-section and a rectangular cross section, given by

$$Correction\ factor,\ Cf = \frac{I_{trapezoidal}}{I_{rectangular}} = \frac{(p+q)(p^2+q^2)}{4h^3} \quad (14)$$

where, p and q are the thickness of the beam at the top and bottom respectively and h is the expected thickness of the beam. This correction factor can be used to estimate the stiffness of a trapezoidal beam, given the stiffness of a rectangular beam with thickness h being given or has been estimated using Eq. (7).

$$K_{corrected} = K_{rectangular} * Cf \quad (15)$$

The correction factor was found to be 2.204 ± 0.637. Using the updated value of stiffness, the maximum actuation force needed to obtain the desired range was estimated to be 48.2 N. Selected VCA with a maximum output force of 116 N will still be adequate for the stage.

2.1.3.3. Noise measurement:. Noise in the stage was measured by collecting displacement data of the center-stage using capacitive sensor for 10 s at a sampling rate of 1000 Hz with no input to the actuators. A high data collection rate ensures that none of the dynamics of the stage are missed. The noise magnitude in the stage was found to be 0.393 ± 0.006 µm. The measured noise is the open loop noise and it can be attenuated in closed loop control of the stage.

2.1.3.4. Parasitic motion:. To obtain the parasitic motion of the stage, the interferometer was mounted collinearly with axis orthogonal and in-plane to the actuation axis. Primary axis was moved through a cyclic range of 49.87 mm starting at −24.98 mm to 24.89 mm. The secondary axis displacement data was collected at a rate of 1000 Hz.

Induced parasitic motion in y-axis is depicted in Fig. 9. It exhibits that the parasitic motion range is ~1723 µm over a travel range of 49.87 mm which corresponds to 3.45% of the primary x-axis motion of the stage. This shows that the two motion axes are decoupled as predicted. This level of coupling between the axes can be effectively eliminated in the closed loop control on both axes.

2.1.3.5. Dynamic performance:. Measuring the open loop dynamic response of the stage is essential to identify the resonant frequency of the stage which sets the bandwidth for an open loop control system and helps in developing a model for the stage (using system identification) which can then be used to develop a robust closed loop control strategy for the stage. A step input voltage signal of magnitude 0.01 V was used to obtain the step response of the stage (see Supplementary Fig. S4). The response function from hereon is defined as the ratio of the actual displacement of the stage to the desired displacement (which is calculated using the stiffness of the stage). The slope shown in Fig. 7 (7701.3 µm/V) is the conversion factor between output displacement and input voltage i.e. a magnitude of 0 dB corresponds to 7701.3 µm of stage motion for a unit input voltage. The step response only seems to

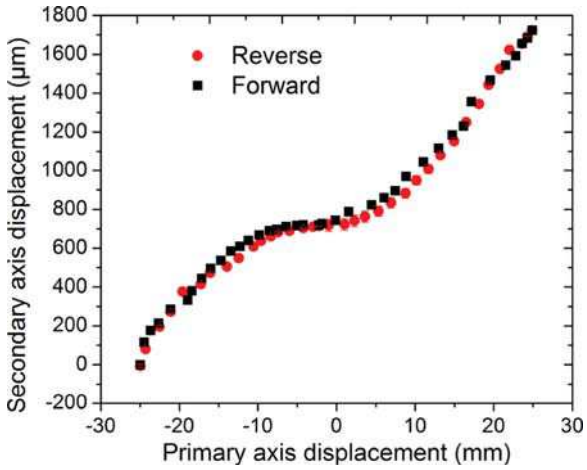

Fig. 9. Graph showing parasitic motion of the stage.

capture the first resonant frequency of the stage which is found to be at 5.6 Hz. To get a more accurate response of the stage over the frequency range, a Gaussian white noise signal with standard deviation- 0.003 V (corresponds to a static displacement of 23.1 µm) was generated at 1000 Hz as the input to the stage and the response was measured using the capacitance probes for a period of 100 s.

The frequency response function was obtained by taking the Fast Fourier transforms of the input and output data. Using the calculated stiffness of the stage, input voltage can be converted to static displacement (displacement at 0 Hz) of the stage. Fig. 10 shows the open loop frequency response function of the stage.

From the magnitude plot, first resonant frequency is observed at 5.2 Hz which matches well with both step response estimate of 5.6 Hz and FEA predicted first resonance at 5.0 Hz. The plot also captures the resonance of the individual double flexure beams between 25 Hz and 40 Hz, which were also obtained with the FEA analysis (modes 3–6, as shown in Fig. 4).

To achieve a bandwidth of 25 Hz for actuation, it is desired to have the uncontrollable resonant frequencies of the stage beyond 25 Hz and preferably at least 2–3 times further. As observed from both FEA and experimental data, resonances of the individual DPFM units are observed in 20 Hz- 40 Hz range. These resonances are a result of the intermediate stages having the same DOF as the main stage leading to additional DOFs in the system. To eliminate these additional DOFs in the system, a modified design for the stage has been developed and will be presented in the next section.

2.2. Modified DPF design

To eliminate the underconstraint from DPF bearings, a nested linkage design (see Fig. 11) has been presented by Panas and Hopkins [24]. Due to nesting of linkage guiding flexures inside the dead space of a regular DPF bearing, the overall footprint of the stage remains the same but since the nested linkage is far from the center of motion it adds inertia equivalent to an external linkage design [23,30]. The parametric design of the nested linkage flexure has been discussed in detail in [24,31]. Due to the design freedom in geometry of these flexures, the range, kinematics, and performance of the main DOF can be designed to desired specifications. This improved linkage design can thus be employed to improve the performance of the DPF stage developed above. Structural and geometric parameters of the design are listed below in Table 2. The thickness of the flexure beams has been reduced to 0.3 mm from 0.5 mm to achieve a similar stiffness as the previous design without increasing the overall footprint of the stage. This helps to ensure that the fundamental resonance frequencies would be comparable making the comparison of higher order resonance

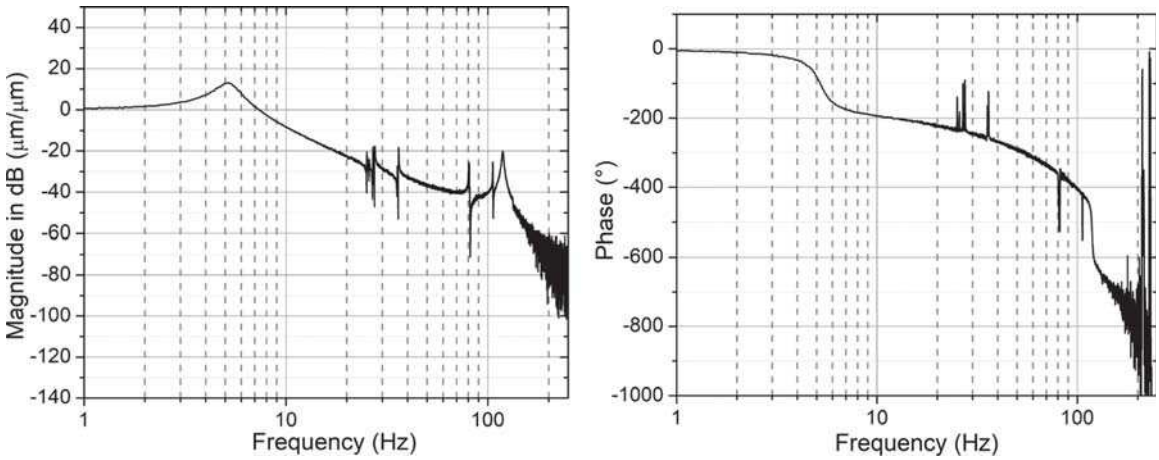

Fig. 10. Magnitude and phase plots of the open loop frequency response of the DPF stage.

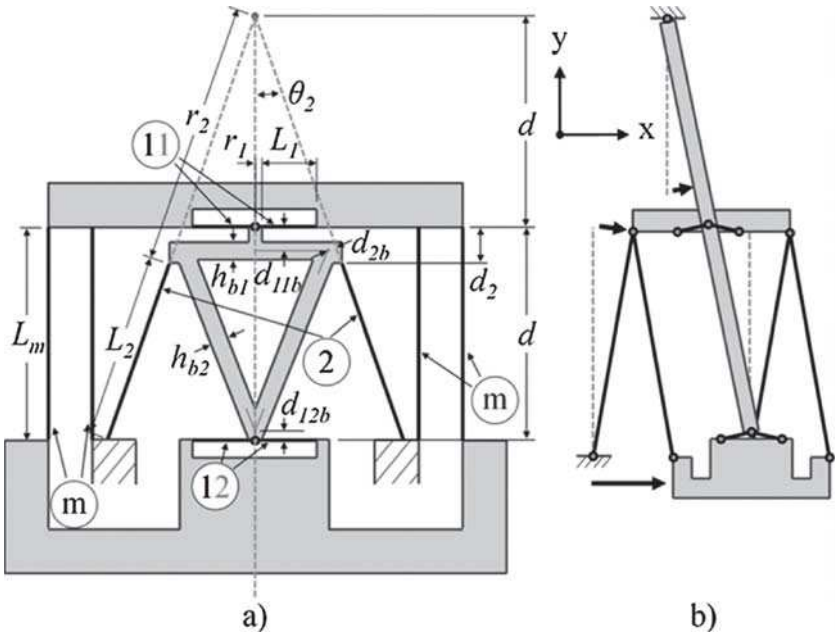

Fig. 11. (a) A nested linkage design with the expected motion for the structure shown in the equivalent linkage model in (b) [24] (Republished with permission of Journal of mechanical design by AMERICAN SOCIETY OF MECHANICAL ENGINEERS, from 'Eliminating Underconstraint in Double Parallelogram Flexure Mechanisms', Panas, R. M., and Hopkins, J. B.,**137**(9), p. 9230, 2015, in the format Republish in a journal/magazine via Copyright Clearance Center, Inc.).

modes between the two designs reasonable.

The tangential stiffness of each such unit is given by

$$k_{ft} = k_{mt} + \frac{k_{1\theta} + \left(\frac{k_{1\theta}}{k_{1t\tau}} + r_1\right)^2 k_{1t}}{d^2} + \frac{k_{2\theta} + \left(\frac{k_{2\theta}}{k_{2t\tau}} + r_2\right)^2 k_{2t}}{2d^2} \tag{16}$$

where,

$$k_{mt} = \frac{(12E_m I_m)}{L_m^3};\ k_{i\theta} = \frac{E_i I_i}{L_i};\ k_{it\tau} = \left(\frac{2E_i I_i}{L_i^2}\right) \tag{17}$$

$$I_i = \frac{bh_i^3}{12};\ I_m = \frac{bh_m^3}{12};\ r_2 = \frac{2d}{\cos\theta_2} - L_2 \tag{19}$$

Since there are 6 such units in parallel (see Fig. 12), aiding the motion along each axis, the overall stiffness of the stage is estimated as

$$k_t = 6k_{ft} \tag{19}$$

Using the geometric and material parameters listed in Table 2, the tangential stiffness of the stage was estimated to be 583 N/m. However, due to tapering in thickness of the beams due to waterjet cutting, this estimate needs to be corrected to account for the change in inertia of the beams. The correction factor estimate was taken to be the same as the correction factor obtained from measurements of DPF stage beams. Using the correction factor of 2.204 ± 0.637 and equation 19, the stiffness of the stage can be estimated to be 1285 ± 371 N/m which overlaps with the experimental stiffness of the DPF stage-1896 ± 265 N/m. An exploded view of the assembly of modified DPF stage has been shown in Fig. 12. The assembly is mounted to the ground through the corner modules on both the top and bottom levels as shown in Fig. 12. To ensure that top module is mounted to the ground, four connector plates are used to connect them to the bottom stage which is then mounted to the ground. The middle flexures at the top module are connected to the center-stage of the bottom level and the middle flexures of the bottom module are connected to the top center-stage. Two VCAs are used for actuation along both x and y axis. The actuation method using VCAs remains the same.

Table 2
Structural and material parameters for modified DPF design.

Parameter	Value	Parameter	Value
L_m	93.6 mm	r_1	1.08
$h_i = h_m$	0.3 mm	θ_2	9.34°
b	12.7 mm	d	93.6 mm
E	71.7 GPa	L_1	31.96 mm
r_2	95.1 mm	L_2	94.61 mm

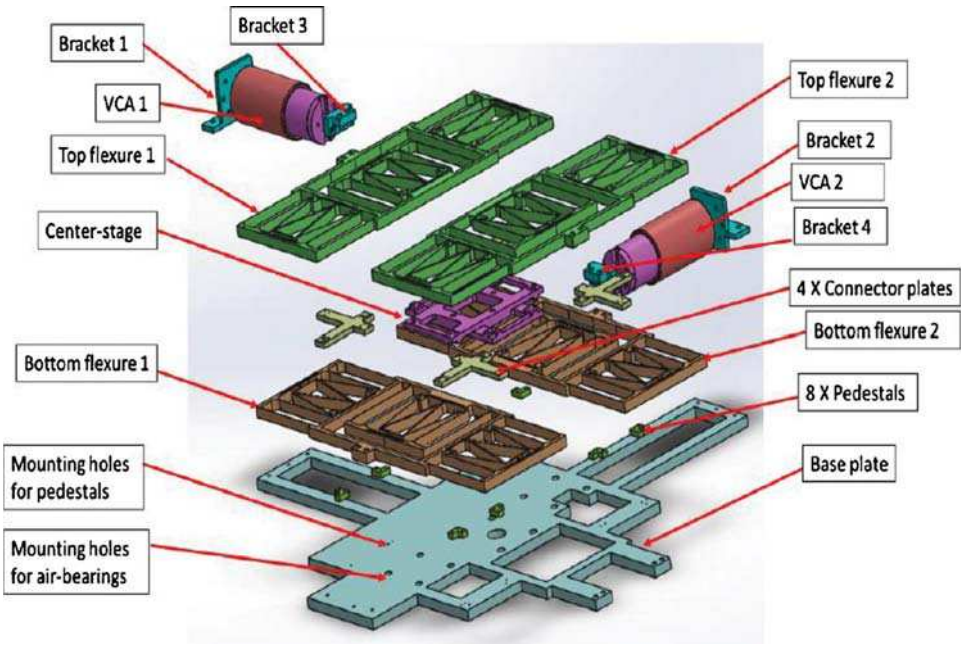

Fig. 12. CAD model of Design 2 of XY stage [25].

2.2.1. FEA results

Each level of the stage is grounded through the holes for connector plates on each corner of the stage level. And the two levels are connected rigidly at the center through the holes for center-stage mounting. One of the two levels are fed an input force value at the voice coil mounting face in the direction of voice coil actuation. The FEA simulation predicted a stiffness of 631 N/m (see Fig. 13) which is lower than the stiffness of DPF stage and thus, maximum force requirement for 50 mm travel is smaller for modified DPF stage and the VCA selected above should be able to produce sufficient actuation force. FEA simulation predicted a maximum stress of 280 MPa at a displacement of 19.3 mm (see Supplementary Fig. S5).The simulation was run without any fillets in the model and with small radius fillet addition (for waterjet cutting), these stresses would be limited [32] as illustrated by stress reduction with fillet addition for DPF design (see Supplementary Figs. S1 and S3). By excluding the few outliers at the corners of the linkage flexures, the maximum stresses in the beam were well under 200 MPa (see Supplementary Fig. S6). Thus, extrapolating this stress to 25.4 mm stage displacement, the maximum stress in the flexures will have an upper bound at 264 MPa. FOS of the design at that stress level is still 1.91.

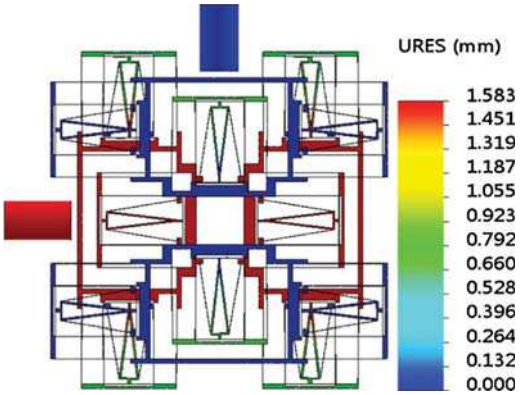

Fig. 13. Static FEA simulation of deformation induced by an input force of 1N.

2.2.2. Physical model

The same physical model as developed for DPF stage has been applied to this stage. Based on the moving mass of the stage and analytical stiffness which were found to be 1.54 kg (takes into account both the mass of the stage and moving mass of voice coil actuator) and 583 N/m, the natural frequency was estimated to be 3.1 Hz. However, dynamic FEA simulation does not include the mass of center-stage and VCAs leading to an inflated FEA estimate of the first resonant frequency. Without including the mass of VCAs and center-stage, the analytical estimate of natural frequency is found to be 4.2 Hz. In addition, the first-six resonant frequencies as predicted by the modal analysis are shown in Fig. 14. The first-two mode shapes as expected are contributed by the translations along the two working axes, respectively. However, the higher modes of this stage are the out of plane resonances of the center-stage instead of the resonances of individual DPFs which cannot be controlled with the two VCAs. These out of plane resonances are beyond our operating range and hence, do not affect the performance of the stage during operation. The next in plane resonance which affects the center-stage occurs at 84.2 Hz which is significantly higher than the corresponding mode observed with FEA of DPF stage (see Fig. 4) showing that the under-constrained dynamics are increased > 3-folds with the use of the nested linkage flexure design. The second resonance of the center-stage is observed at 129 Hz (Fig. 15).

2.2.3. Experimental results

Setup for testing of the modified DPF stage remains the same as that used for DPF stage (see Fig. 16) (Fig. 16–18).

2.2.3.1. Stiffness measurement:. The same procedure that was used to measure the stiffness of the DPF stage was also used to measure the stiffness of the modified DPF stage. The small displacement stiffness of the stage was calculated from the slope of the displacement of the stage vs input voltage graph and was found to be 1158 ± 162 N/m (Fig. 17). This is almost twice the stiffness predicted by static FEA analysis. As expected, the variability in thickness of the beam causes a significant change in stiffness of the beam. To verify this effect, measurements were taken for the thickness of the beam. Using a set of 40 measurements for each thickness estimate, the thickness at the top of the beam was measured to be 0.26 ± 0.05 mm and at the bottom of the

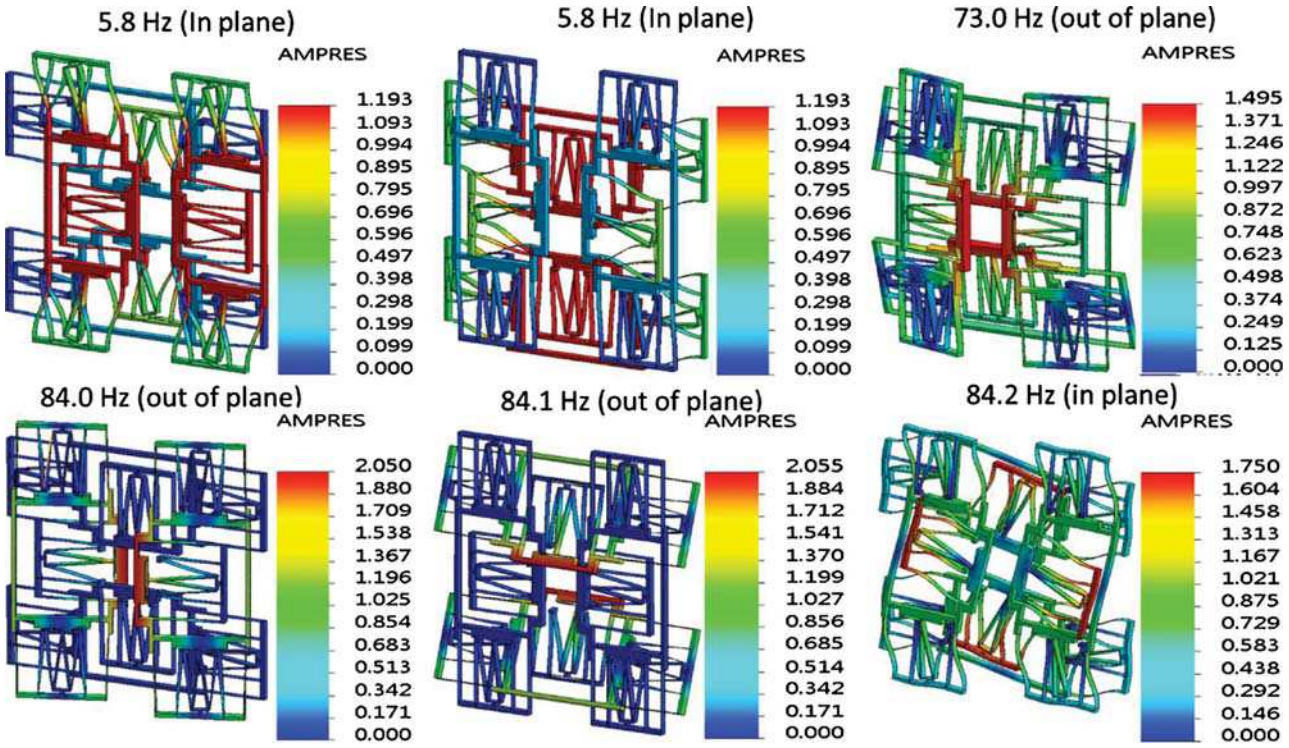

Fig. 14. First-six resonant mode shapes and resonance frequencies of the design 2 of XY stage.

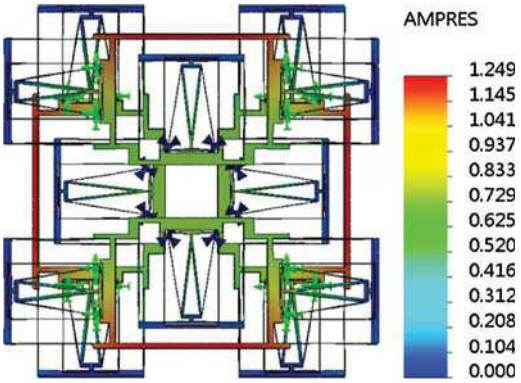

Fig. 15. Second resonance of the center-stage.

beam, it was found to be 0.52 ± 0.06 mm. Using equation 14, the correction factor was obtained as 2.41 ± 0.72 and the corrected stiffness (using FEA) was estimated using equation 15 and was found to be 1520 ± 454 N/m. Using the null hypothesis that corrected FEA estimate and experimentally obtained stiffness estimates are the same, the z statistic was found to be −0.0702. With a test statistic of −0.0702 and a rejection region of {z > 1.96 or z < −1.96} at a 5% level of significance, we do not have enough statistical evidence to reject the null hypothesis i.e. the two parameters are the same. (see Supplementary Information S3 for details of the hypothesis testing of the two quantities).

2.2.3.2. Noise measurement:. From the zero-input data of the stage, noise in the stage was estimated to be 0.106 ± 0.008 μm. Using a power supply with sufficient input voltage resolution, a resolution of a

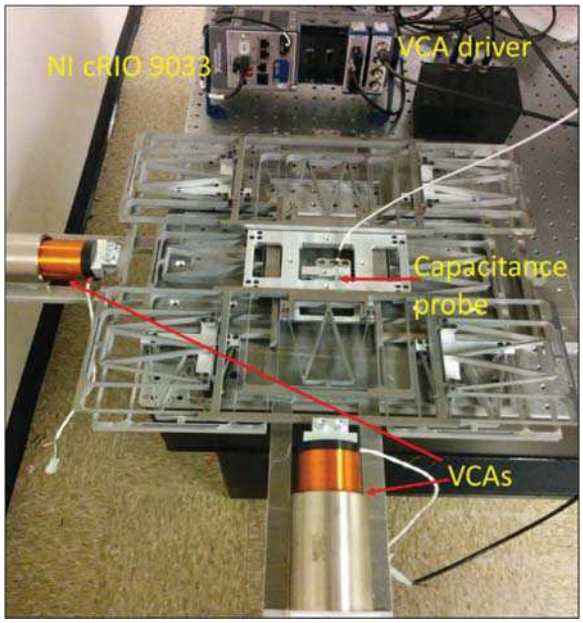

Fig. 16. Experimental setup for modified DPF design.

100 nm can be obtained in open loop with a 1:1 signal to noise ratio. However, this resolution can be improved even further when the stage is operated with a closed loop control.

2.2.3.3. Parasitic motion:. For obtaining the parasitic motion of the stage, the primary axis was moved through a travel range from −27.80 mm to 27.49 mm and the secondary axis displacement was

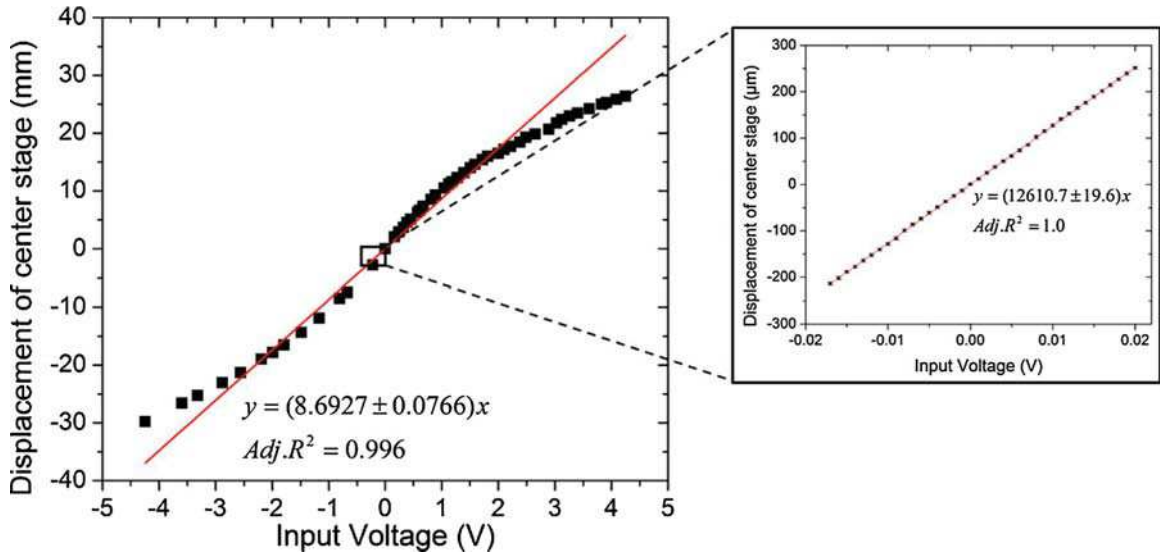

Fig. 17. Displacement vs input voltage for modified DPF.

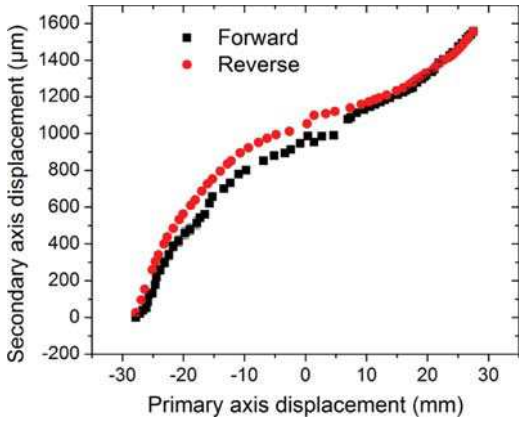

Fig. 18. Parasitic motion of modified DPF.

measured using the interferometer.

The parasitic motion range along secondary axis is found to be ~1557 μm over a travel range of 54.29 mm which corresponds to 2.87% of the primary x-axis motion of the stage (Fig. 18).

2.2.3.4. Dynamic performance – step response:. First resonant frequency of the stage was found to be at 4.4 Hz (see Supplementary Fig. S8 for step response of the stage) which is in between the estimated resonant frequency of 3.1 Hz (uses non-corrected analytical stiffness) and the FEA predicted resonance of 5.8 Hz. This difference could be explained by the fact that the dynamic FEA simulations did not consider the moving mass of voice coil actuators and the center-stage which increased their resonant frequency prediction. Both the analytical and FEA estimates need to be corrected to account for the manufacturing error tolerance and errors in moving mass estimation. The corrected estimates have been included in the discussion section.

2.2.3.4.1. Gaussian white noise response:. A Gaussian white noise with a standard deviation 0.0035 V (which translates to a static displacement of 44.1 μm) was input to the stage and data was collected for 100 s at a sampling rate of 1000 Hz 0 dB magnitude corresponds to a 12610.7 μm motion of center stage for every unit input voltage. Magnitude plot shown in Fig. 19 represents the magnitude of ratio of actual displacement and static displacement.

First resonant frequency of the stage was obtained at 4.2 Hz which is close to the predicted estimate of natural frequency of the stage. Resonances of the intermediate stage which propagated to the main stage with DPF stage were moved out and the first of them was obtained at 86 Hz.

3. Discussion

Based on the FEA analysis, static and dynamic experiments conducted on DPF stage and modified DPF stage, the stiffness and natural frequencies of the two stages have been listed in Table 3. The values represented in the table are *mean ± standard deviation* of the corresponding parameter. For a 95% confidence interval of the parameter estimate, use *mean ± 2* standard deviation.* Due to the manufacturing defects introduced by waterjet cutting of stages, a correction factor to account for the change in inertia of the beams had to be incorporated into the models to get an accurate understanding of the true dynamics of the fabricated beams. On incorporating the correction factors into the model and FEA estimates of the stiffness (see Supplementary Information S1), the analytically predicted stiffnesses of the two stages were shown to be in good agreement with the FEA simulated stiffnesses. The mean corrected FEA estimate and mean corrected analytical estimate were within 3.1% and 2.2% error of the mean experimental stiffness respectively. For the modified DPF stage, these error limits were found to be 31.2% for FEA estimate and 21.3% for analytical estimate. However, the experimental stiffness obtained was within the one-sigma limit of the corrected analytical estimate. Based on the hypothesis testing to determine the equality of mean FEA and mean experimental estimate of modified DPF stage's stiffness (see hypothesis testing in Supplementary Information S3) with a 5% significance level (reject null hypothesis if $Z > 1.96$ or $Z < -1.96$), the z-statistic for the null hypothesis that the FEA estimate and experimental stiffness are the same is 0.751 (see Table 4) and thus, there is not enough statistical evidence to reject the null hypothesis. In other words, they are the same. Similarly, the z-statistic for the null hypothesis that the analytical estimate and experimental stiffness for the modified DPF stage are the same is 0.549 and thus, not enough statistical evidence to reject the null hypothesis.

For resonant frequency estimates, the moving mass for DPF and modified DPF were estimated to be 1.46 kg and 1.54 kg respectively. Since the FEA dynamic solution did not take into account the true moving mass of VCAs and the mass of center-stage in the modified DPF case, those frequency estimates had to be corrected accordingly (see Supplementary Information S1 for details). For natural frequency estimates, a simple spring-mass model was used. From the z-statistic for

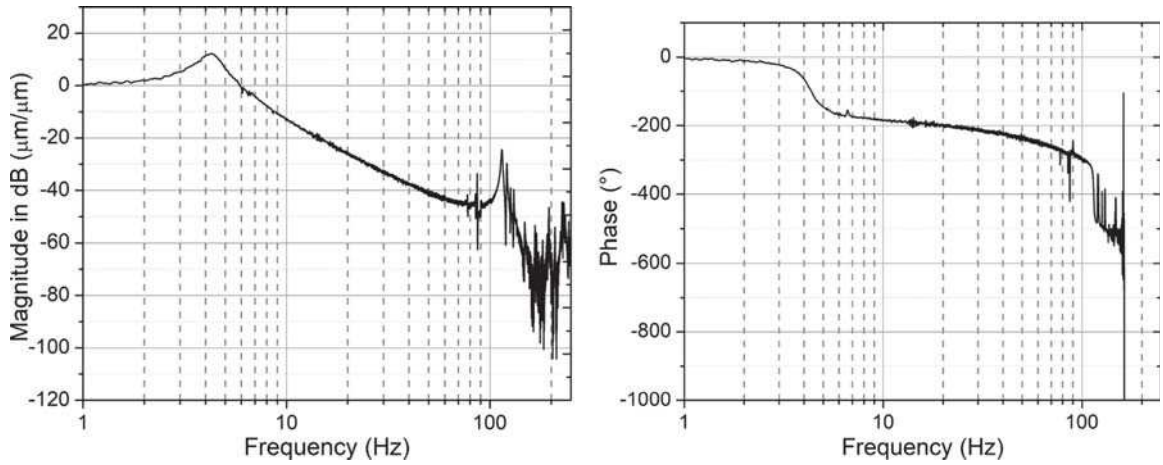

Fig. 19. Magnitude and phase plots of the open loop Gaussian white noise response of the modified DPF stage.

Table 3
Comparison of the stiffness and natural frequency estimates (Analytical and FEA) with experimental estimates for both DPF and modified DPF stages.

		Corrected FEA estimate	Corrected Analytical Estimate	Experimental
DPF stage	k (N/m)	1854 ± 536	1836 ± 531	1896 ± 265
	ω_n (Hz)	5.3 ± 0.8	5.6 ± 0.8	5.2 ± 0.0
Modified DPF stage	k (N/m)	1520 ± 454	1405 ± 420	1158 ± 162
	ω_n (Hz)	6.7 ± 1.0	4.8 ± 0.7	4.2 ± 0.0

Table 4
Z-statistic for comparison of mean stiffness and mean frequency estimates for all possible pairs (FEA, Analytical and Experimental) of both DPF and modified DPF stages.

		$Z_{FEA\text{-}Analytical}$	$Z_{Analytical\text{-}Experimental}$	$Z_{FEA\text{-}Experimental}$
DPF stage	k	0.0238	−0.1011	−0.0702
	ω_n	−0.2652	0.5000	0.1250
Modified DPF stage	k	0.1859	0.5487	0.7510
	ω_n	1.5565	0.8571	2.5

natural frequency estimates of DPF stage, all the possible pairs are found to be in good agreement with one another with 5% significance level. For the modified DPF stage, there is sufficient evidence to reject the null hypothesis that mean FEA resonant frequency is the same as the mean experimental frequency estimate. This discrepancy could be attributed to the estimation errors in moving mass calculation for resonance frequency correction.

3.1. Range and open loop resolution

Stress developed at 25.92 mm displacement of DPF stage was found to be 182 MPa which computes to a factor of safety of 2.76 and the stage has been shown experimentally to have a reachable workspace of 50 mm × 50 mm. For the modified DPF stage, the stress at a displacement of 19.2 mm was found to be 200 MPa. Using the linearity of stress-strain curve, the stress computed at a displacement of 25.4 mm was found to be 264 MPa which equates to a factor of safety of 1.91. Even on including the effect of manufacturing error on the stresses developed in the designs (see Supplementary Information S2 for stress change calculation due to manufacturing errors), the FOSs were found to be 1.89 and 1.10 for DPF and modified DPF stage designs respectively. Thus, both stages should achieve the desired range of 50 mm without encountering any plastic deformation of the beams and this has been validated experimentally. In open loop operation, the resolution of stage is limited by the noise in the stage. Using an SNR of 1, the resolution of DPF stage in open loop was obtained as 396 ± 6.00 nm while that of the modified DPF stage was found to be 106 ± 8 nm. Modified stage thus provides an improvement in the resolution of the stage, likely due to its reduction in higher order unconstrained modes of vibration.

Based on the modal analysis of the stages, the first uncontrollable mode for DPF stage was encountered at 19.2 Hz while the first uncontrollable mode was encountered at 84.2 Hz with modified DPF stage. This has been corroborated by the experimental results which show the uncontrollable mode move out from 25.2 Hz to 86 Hz (see Fig. 20). The next mode for DPF stage which affects the center-stage was observed at 119 Hz and that for the modified DPF stage was found at 115 Hz. Both of these were found to be in good agreement with the FEA predicted results. It is also expected for these modes to be close to each other as the overall stiffness and masses of the two stages are close to one another.

Table 5 lists the resonant frequencies of the two stages based on FEA results and classifies them into controllable (in plane and center-stage) and uncontrollable resonances (in-plane & uncontrollable and out of plane). From the table, it can be observed that the first uncontrollable mode has moved out from 19.2 Hz to 84.2 Hz.

Future work includes model identification and developing a robust control scheme for the system using the model. The controller should improve the bandwidth of the stage by damping out the resonance present in the system without affecting the static performance of the system and achieve the desired bandwidth.

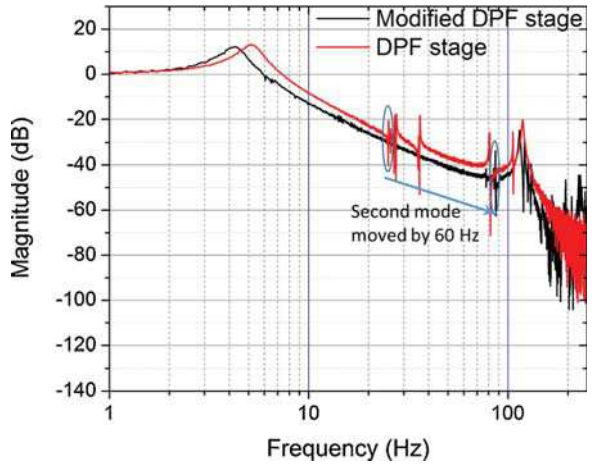

Fig. 20. Comparison of the magnitude response plots for DPF (0 dB = 7701.3 μm center stage motion for 1 V input) and modified DPF stages (0 dB = 12610.7 μm center stage motion/V).

Table 5
Comparison of the modal analysis of DPF and modified DPF stages.

	Frequency (Hz)	
Mode no.	DPF stage	Modified DPF stage
1	4.10 (+)	5.80 (+)
2	4.10 (+)	5.80 (+)
3	19.16 (−)	72.97 (X)
4	19.22 (−)	84.03 (X)
5	21.51 (−)	84.07 (X)
6	21.76 (−)	84.18 (−)

+ In plane & controllable.
X Out of plane.
− In plane and uncontrollable.

4. Conclusion

In this paper, the design, fabrication, and testing of a XY nano-positioning stage with a range of 50 mm in each working direction of the stage has been presented. Both FEA results and experimental results show that a working range of range of 50 mm along both axes is easily obtained using a DPF design for the stage. In addition, the static results for the DPF design showed that this design is capable of achieving an open loop resolution of 400 nm and a static coupling of less than 3.5% between the two axes over its entire range.

A modified DPF stage design was also presented to shift the parasitic uncontrollable resonances of the DPF stage beyond a desired working bandwidth of 25 Hz. Both FEA and experimental results show that the uncontrollable modes were moved out from ~25 Hz to ~86 Hz without significantly affecting the resonance of the center-stage. Static cross-talk between the two stages was found to be smaller than 2.9%, thus suggesting an effective decoupling between the motions along the two axes. The resolution of the stage was found to be 100 nm in open loop operation. Thus, this modified DPF design shows a significant improvement in dynamic performance and resolution as compared with the regular DPF design without resulting in any increase in the footprint of the stage or loss of axis decoupling.

Acknowledgements

The authors would like to acknowledge the financial support received from NXP Semiconductors. The authors would like to thank Butch Cunningham, UT Austin for the waterjet cutting of the flexure units and Mr. CS Foong- NXP Semiconductors for his CAD models of the base plates and valuable inputs to the discussion on assembly of the stage.

Appendix A. Supplementary data

Supplementary data associated with this article can be found, in the online version, at https://doi.org/10.1016/j.precisioneng.2018.04.007.

References

[1] Wagner C, Harned N. EUV lithography: lithography gets extreme. Nat Photonics 2010;4(1):24–6.
[2] Choi K-B, Lee JJ. Passive compliant wafer stage for single-step nano-imprint lithography. Rev Sci Instrum 2005;76(7):75106.
[3] Hausotte T, Jaeger G, Manske E, Hofmann N, Dorozhovets N. Application of a positioning and measuring machine for metrological long-range scanning force microscopy. Opt Photonics 2005;2005:587802.
[4] Kwon J, Hong J, Kim Y-S, Lee D-Y, Lee K, Lee S, et al. Atomic force microscope with improved scan accuracy, scan speed, and optical vision. Rev Sci Instrum 2003;74(10):4378–83.
[5] O'Brien W. Long-range motion with nanometer precision. Photonics Spectra 2005;39(6):80–1.
[6] Gonda S, Kurosawa T, Tanimura Y. Mechanical performances of a symmetrical, monolithic three-dimensional fine-motion stage for nanometrology. Meas Sci Technol 1999;10(11):986.
[7] Huang HB, Sun D, Mills JK, Cheng SH. Robotic cell injection system with position and force control: toward automatic batch biomanipulation. IEEE Trans Robot 2009;25(3):727–37.
[8] Roy NK, Foong CS, Cullinan MA. Design of a micro-scale selective laser sintering system. 2016 Annual International Solid Freeform Fabrication Symposium 2016:1495–508.
[9] Ding H, Xiong Z. Motion stages for electronic packaging design and control. IEEE Robot Autom Mag 2006;13(4):51–61.
[10] Culpepper ML, Anderson G. Design of a low-cost nano-manipulator which utilizes a monolithic, spatial compliant mechanism. Precis Eng 2004;28(4):469–82.
[11] Xu Q. Design and development of a compact flexure-based $ XY $ precision positioning system with centimeter range. IEEE Trans Ind Electron 2013;61(2):893–903.
[12] Awtar S, Parmar G. Design of a large range XY nanopositioning system. J Mech Robot 2013;5(2):21008.
[13] Kang D, Kim K, Kim D, Shim J, Gweon D-G, Jeong J. Optimal design of high precision XY-scanner with nanometer-level resolution and millimeter-level working range. Mechatronics 2009;19(4):562–70.
[14] Slocum AH. Precision machine design. Society of Manufacturing Engineers; 1992.
[15] Smith ST. Flexures: elements of elastic mechanisms. CRC Press; 2000.
[16] Kim W, Verma S, Shakir H. Design and precision construction of novel magnetic-levitation-based multi-axis nanoscale positioning systems. Precis Eng 2007;31(4):337–50.
[17] Kenton BJ, Leang KK. Design and control of a three-axis serial-kinematic high-bandwidth nanopositioner. IEEE/ASME Trans Mechatron 2012;17(2):356–69.
[18] Ru C, Liu X, Sun Y. Nanopositioning Technologies: Fundamentals and Applications. Springer; 2015.
[19] Fleming AJ, Leang KK. Design, modeling and control of nanopositioning systems. Springer; 2014.
[20] Awtar S, Slocum AH, Sevincer E. Characteristics of beam-Based flexure modules. J Mech Des 2007;129(6):625.
[21] Awtar S. Synthesis and analysis of parallel Kinematic XY flexure mechanisms, Doctoral dissertation. Massachusetts Institute of Technology; 2004.
[22] Trutna TT, Awtar S. An enhanced stability model for electrostatic comb-drive actuator design. ASME 2010 International Design Engineering Technical Conferences and Computers and Information in Engineering Conference 2010:597–605.
[23] Brouwer DM, Otten A, Engelen JBC, Krijnen B, Soemers H. Long-range elastic guidance mechanisms for electrostatic comb-drive actuators. Proceedings of the Euspen Intenational Conference. 2010. p. 41–50.
[24] Panas RM, Hopkins JB. Eliminating underconstraint in double parallelogram flexure mechanisms. J Mech Des 2015;137(9):92301.
[25] Roy NK, Cullinan MA. Design of a flexure based xy precision nanopositioner with a two inch travel range for micro-scale selective laser sintering. Proceedings − ASPE 2016 Annual Meeting. 2016. p. 395–400.
[26] Xu Q. Design and development of a compact flexure-based XY precision positioning system with centimeter range. IEEE Trans Ind Electron 2014;61(2):893–903.
[27] Yang Y, Wei Y, Lou J, Xie F. Design and analysis of a new flexure-based XY stage. J Intell Mater Syst Struct 2017;28(17):2388–402.
[28] Moheimani SOR. A survey of recent innovations in vibration damping and control using shunted piezoelectric transducers. IEEE Trans Control Syst Technol 2003;11(4):482–94.
[29] IBS Precision Engineering, Data sheet − LION Precision capacitive sensors [Online]. Available: http://www.ibspe.com/public/uploads/content/files/capacitive-data-sheet-EN.pdf. [Accessed: 05-Sep-2017].
[30] Brouwer DM. Design principles for six degrees-of-freedom MEMS-based precision manipulators. Twente University Press; 2007.
[31] Panas RM. Large displacement behavior of double parallelogram flexure mechanisms with underconstraint eliminators. Precis Eng 2016;46:399–408.
[32] Tipton SM, Sorem JR, Rolovic RD. Updated stress concentration factors for filleted shafts in bending and tension. J Mech Des 1996;118(3):321–7.